

<https://doi.org/10.1038/s44304-025-00134-y>

# Rising temperatures intensify drought propagation and severity across the contiguous United States

Check for updates

Hongxiang Yan , Ning Sun, Lili Yao, Travis B. Thurber &amp; Jennie S. Rice

Droughts can propagate from meteorological droughts (MD) into agricultural (AD) and hydrological droughts (HD). However, the mechanisms by which rising temperatures and changes in precipitation amount influence MD propagation, and how these dynamics vary across U.S., are not yet fully understood. This gap is critical given the U.S.'s diverse climates and land-use patterns, which lead to region-specific drought vulnerabilities and impacts, such as the 2012 AD in the Great Plains and the 2014 HD in the western U.S. Using a dynamical-statistical framework, we assess warming impacts on drought propagation. Results reveal that the Midwest and Southeast, key agricultural regions, show the largest increases in MD propagation to AD/HD, driven by rising temperatures and declining precipitation, though magnitudes vary regionally. In contrast, the Northeast shows reduced propagation due to increased year-round precipitation. Higher-intensity AD/HD events become disproportionately more likely, with rates varying by region and MD intensity.

Drought represents a multifaceted natural hazard with profound and far-reaching impacts on agriculture, ecosystems, and socioeconomic systems<sup>1–4</sup>. Traditionally, droughts are categorized into four distinct types<sup>5</sup>: meteorological (MD), agricultural (AD), hydrological (HD), and socioeconomic drought. Each category highlights a specific domain of drought impact, ranging from reduced precipitation to water supply shortages and economic disruptions due to water scarcity. Importantly, these drought types are not isolated but interconnected, often cascading from one form to another through a process termed drought propagation<sup>6–8</sup> (illustrated schematically in Fig. 1a). MD, defined by prolonged periods of below-average precipitation and often elevated atmospheric water demand, typically serves as the precursor to other drought types. For instance, MD can trigger AD when soil moisture becomes insufficient for crops, which may then progress to HD as reduced runoff diminishes water supplies in reservoirs, rivers, and aquifers. However, the probabilities and dynamics of drought propagation can vary by region, as regional factors determine whether MD is more likely to propagate to AD or HD. Studies have highlighted the complexity of these processes, pointing to the critical role of watershed storage, base flow rates, climate aridity, and human activities in modulating drought propagation dynamics<sup>9–17</sup>.

Despite significant advances, a critical gap remains in understanding how rising temperatures and changes in precipitation amount may influence the likelihood of MD propagating into AD or HD, and how these dynamics vary across the Contiguous U.S. (CONUS) (Fig. 1b, d). This knowledge is essential for identifying at-risk regions of drought and guiding

effective management strategies<sup>18–21</sup>. Under rising temperatures<sup>22</sup>, drought propagation dynamics are poised to evolve in complex and unprecedented ways. Higher temperatures will likely intensify evaporation, accelerate soil moisture depletion, and diminish snowpack, collectively altering the frequency, intensity, and duration of drought events<sup>23–26</sup>. These changes are expected to increase the likelihood of MD propagating into more AD or HD, particularly in regions prone to rapid soil moisture depletion<sup>27–29</sup>. However, regional variability in precipitation patterns, soil properties, and hydrological responses complicates this relationship, with some areas potentially experiencing reduced drought risk due to increased precipitation<sup>30,31</sup>. Understanding these regional differences is critical for tailoring management strategies and improving drought resilience. Yet, large-scale drought studies often rely on land surface models (LSMs) whose calibration specific to drought propagation dynamics may be limited<sup>32–38</sup>, potentially compromising the reliability of drought projections<sup>39–42</sup>.

This study bridges these gaps by systematically assessing how thermodynamic warming may influence drought propagation probabilities across the CONUS, using a well-calibrated LSM tailored for hydrological simulation. We investigate how different MD intensities lead to varying AD/HD intensities, while also identifying regions where warming exacerbates or mitigates these probabilities. Meteorological forcing uses the 12-km Weather Research and Forecasting (WRF) Thermodynamic Global Warming (TGW) dataset<sup>43</sup>, which includes dynamically downscaled fifth generation of European Reanalysis (ERA5) dataset<sup>44</sup> as the historical baseline. Future projections are generated using perturbed thermodynamics

Pacific Northwest National Laboratory, Richland, WA, USA. ✉e-mail: [hongxiang.yan@pnnl.gov](mailto:hongxiang.yan@pnnl.gov)

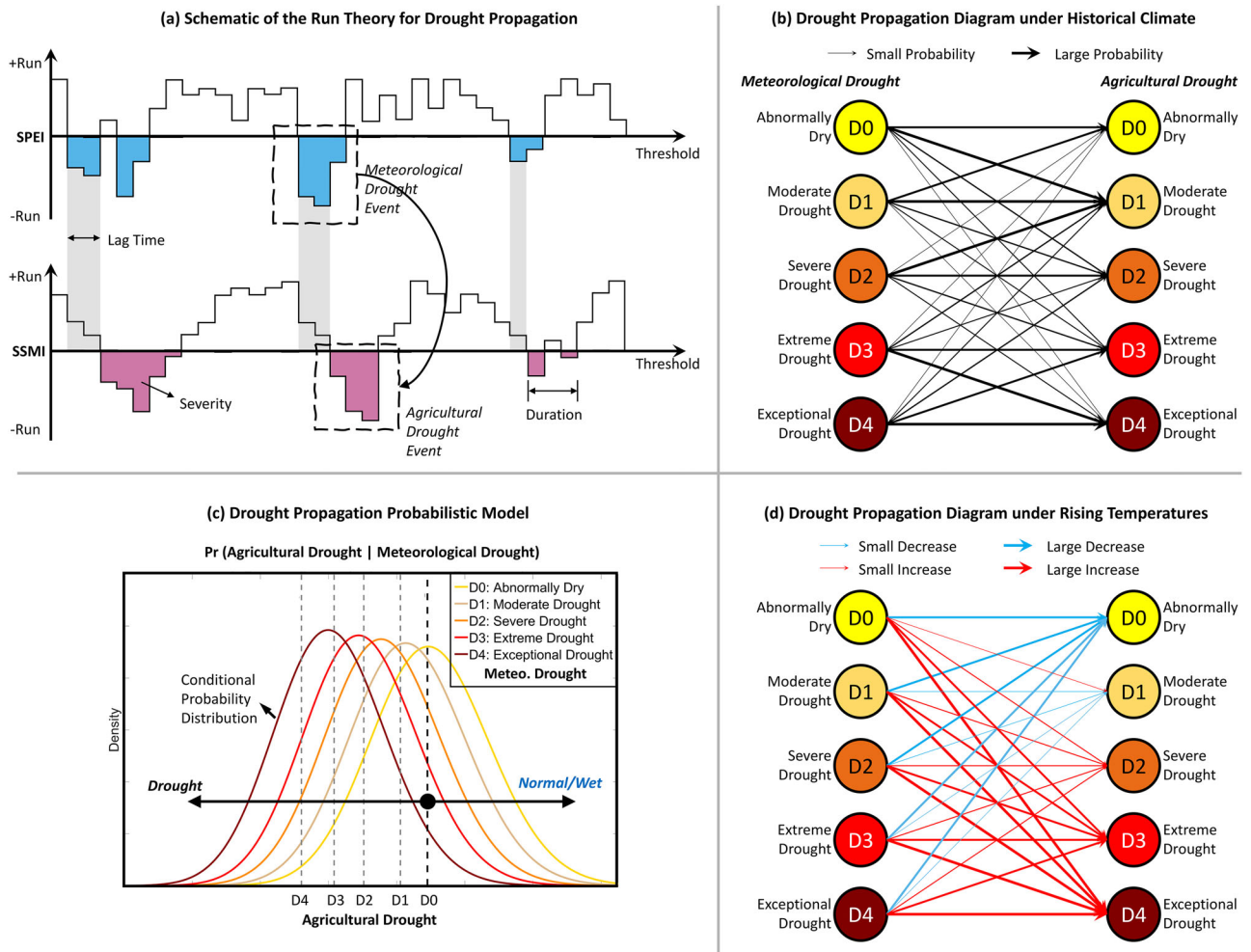


**Fig. 1 | Illustration of drought characterization and propagation processes.** **a** Schematic representation of the run theory applied to drought propagation, using meteorological drought (MD, defined by the Standardized Precipitation Evapotranspiration Index, SPEI) and agricultural drought (AD, defined by the Standardized Soil Moisture Index, SSMI) as an example. **b** Diagram showing how MD events of varying intensity propagate to AD events under historical climate conditions. The probability of propagation varies with MD intensity. This example is illustrative; actual probabilities may differ by region—details are provided in the main text. Drought intensities follow the five-category

classification of the U.S. Drought Monitor (USDM)<sup>3</sup>. **c** Probabilistic drought propagation model, showing five conditional probability density functions (PDFs) that represent the likelihood of AD intensities given a specific MD intensity. **d** Example of changes in drought propagation under rising temperatures. This study suggests a reduced probability of low-intensity AD and an increased probability of high-intensity AD. This illustrative example focuses on MD-to-AD propagation; actual regional responses and other pathways (e.g., MD to HD) may vary and are discussed in the main text.

experiments, which modify the historical weather patterns with projected changes in temperature and other thermodynamic variables (e.g., specific humidity and sea surface temperature) derived from a multi-model ensemble of Coupled Model Intercomparison Project Phase 6 (CMIP6) global climate models (GCMs). This approach—used in the TGW simulations—preserves the dynamical consistency of observed historical weather while assessing how past extreme events, such as droughts, might evolve under perturbed thermodynamic conditions. The projections are based on two CMIP6 greenhouse gas emissions scenarios: SSP245 and SSP585.

TGW are integrated with the well-calibrated Community Land Model version 5 (CLM5)<sup>45–47</sup>, a state-of-the-art LSM to predict hydrology across 464 CAMELS (Catchment Attributes and Meteorology for Large-sample Studies)<sup>48,49</sup> basins across the CONUS. The hydrological outputs from CLM5 are used to characterize drought events, employing the Standardized Precipitation Evapotranspiration Index (SPEI)<sup>50</sup> for MD, the Standardized Soil Moisture Index (SSMI)<sup>51</sup> for AD, and the Standardized Runoff Index (SRI)<sup>52</sup> for HD. These identified drought events serve as the foundation for developing a probabilistic drought propagation model using Bayesian networks<sup>53,54</sup>, enabling a detailed analysis of shifting drought propagation

under warming scenarios (Fig. 1c). The Bayesian networks are well-suited for this analysis due to their ability to effectively model conditional probabilities<sup>53,55,56</sup>.

## Results and discussion

### Shifting drought characteristics

We calibrated CLM5 for each basin individually based on the basin outlet observed streamflow<sup>48</sup>, using the Kling-Gupta efficiency (KGE) metric<sup>57</sup>. Supplementary Fig. 1 shows the KGE values for each basin using both default and calibrated hydrological parameters. The results indicate that the calibrated parameters substantially improve the default runoff simulations across the CONUS, with the most significant improvements observed in more arid parts of CONUS, including the Great Plains and portions of the Midwest region as defined in this study (Fig. 2a1). Following CLM5 model calibration, we conduct simulations for each basin under both historical and eight scenarios provided by TGW (2 scenario × 2 warming signal × 2 future period): SSP245COOLER\_NEAR, SSP245COOLER\_FAR, SSP245HOTTER\_NEAR, SSP245HOTTER\_FAR, SSP585COOLER\_NEAR, SSP585COOLER\_FAR, SSP585HOTTER\_NEAR, and SSP585HOTTER\_FAR.

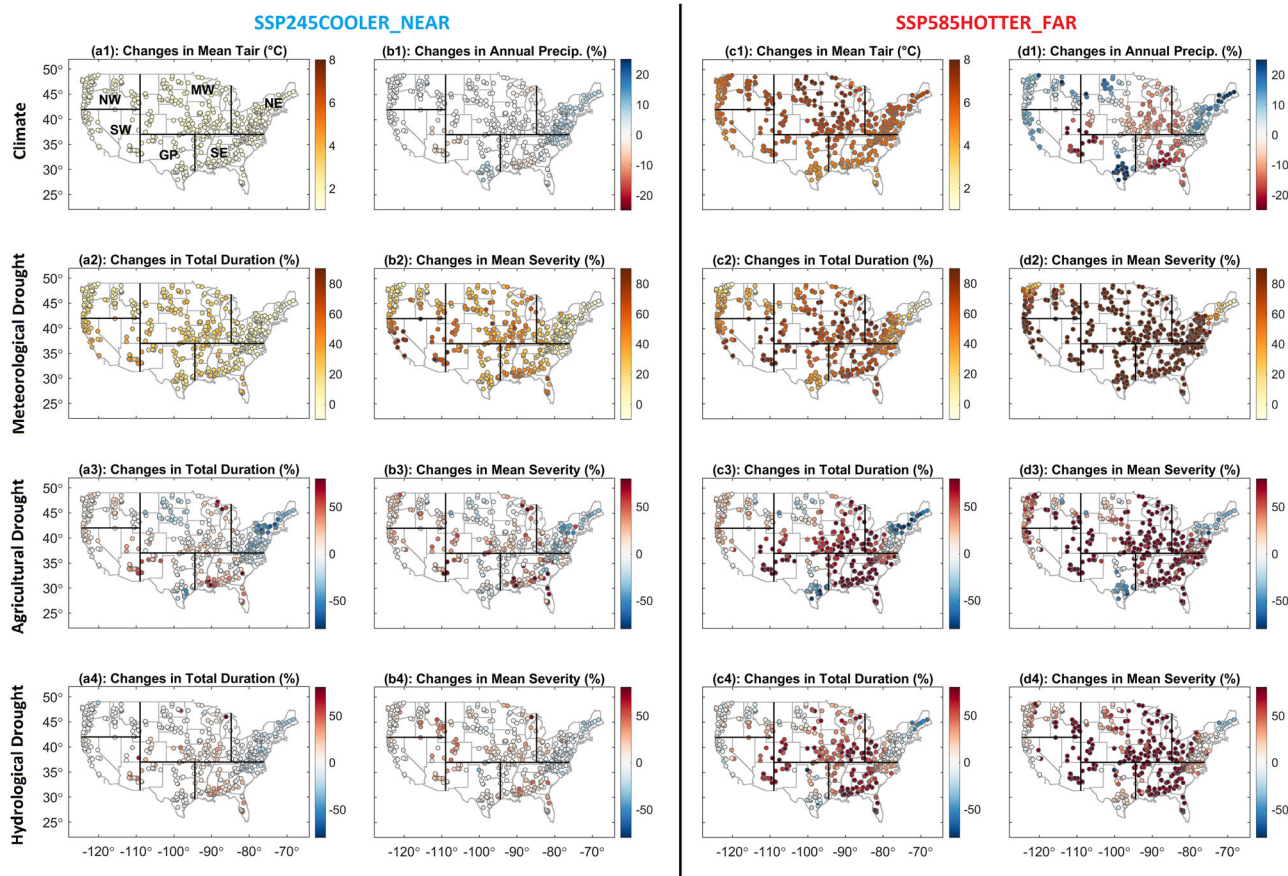


**Fig. 2 | Changes in precipitation, air temperature, and drought characteristics across each basin in the CONUS.** Two scenarios with the least (SSP245COOLER\_NEAR) and most (SSP585HOTTER\_FAR) impacts are shown here as examples. Basins are divided into six regions for the regional analysis. **a1–d1** Warming impacts on mean air temperature and annual precipitation. **a2–d2** Warming impacts on MD characteristics (total duration and mean severity). **a3–d3** Warming

impacts on AD characteristics. **a4–d4** Warming impacts on HD characteristics. Note that the air temperature and precipitation changes shown are mean annual values; seasonal patterns can differ significantly. For example, in the SW, projections indicate wetter winters and drier summers. See Supplementary Figs. 2–5 for seasonal air temperature and precipitation changes.

To distinguish drought dynamics across different hydrometeorological conditions, we grouped the 464 CAMELS basins into six regions for regional analysis across the CONUS, following the classification by Xia et al.<sup>58</sup> (Fig. 2a1): Northwest (NW), Southwest (SW), Midwest (MW), Great Plains (GP), Northeast (NE), and Southeast (SE). Figure 2 illustrates the changes in precipitation, air temperature, and drought characteristics between the historical period and two thermodynamic warming scenarios that represent the least and most extreme cases: SSP245COOLER\_NEAR and SSP585HOTTER\_FAR. Under both scenarios, widespread temperature increases are projected across the CONUS, though with notable regional variations. The most significant warming is observed in the MW, where temperatures rise by 1.7 °C under SSP245COOLER\_NEAR and by 6.9 °C under SSP585HOTTER\_FAR. Detailed changes in monthly and annual mean air temperature for each region and all future scenarios are provided in Supplementary Figs. 2–5. Across all regions, the warm season experiences a greater temperature increase than the cold season, indicating a higher frequency of extremely hot days in the future. Annual precipitation projections show an overall increase in the NW, GP, and NE, with respective increases of 6.9%, 8.5%, and 6.3% under the SSP585HOTTER\_FAR scenario. In contrast, precipitation decreases in the MW and SE, with reductions of –6.2% and –11.0%, respectively, under the same scenario. These changes, however, exhibit significant monthly variability (Supplementary Fig. 4). Regions with strong precipitation seasonality, such as the NW, SW, and GP, experience most of their precipitation increases during the cold season, while the warm season sees minimal increases or even declines. In contrast, the NE, which has the lowest precipitation seasonality across the

CONUS, exhibits a relatively consistent precipitation increase across both cold and warm seasons.

As shown in Fig. 2, despite projected increases in annual precipitation in some regions, all regions experience longer MD total duration and greater mean severity (i.e., longer-lasting and more intense). This suggests that rising temperatures, likely through enhanced potential evapotranspiration (PET), play a significant role in intensifying MD characteristics, even offsetting the effects of increased precipitation in some regions. This underscores the importance of incorporating temperature in characterizing MD. Supplementary Fig. 6 presents the frequency of MD in each calendar month for both the historical period and the eight future scenarios. Across all six regions, MD increases more significantly during the warm season than the cold season, aligning with the fact that temperature increases are more pronounced in the warm season. For example, in the MW region under the SSP585HOTTER\_FAR scenario, the occurrence probability of MD is projected to increase from 0.32 under historical conditions to 0.95 in August and from 0.34 to 0.37 in January. The compounded effects of higher temperatures and reduced precipitation result in the largest MD increases in the SW, MW, and SE, with total durations and mean severities increasing by up to 70% and 400%, respectively, under the SSP585HOTTER\_FAR scenario.

A similar pattern is observed for AD and HD in monthly frequency, with the warm season showing a greater increase in AD and HD frequency than the cold season. However, in some regions, such as NW, where precipitation is increasing, AD and HD decrease in the cold season but increase in the warm season (Supplementary Figs. 7 and 8). In contrast to MD, changes in the duration and severity of AD and HD

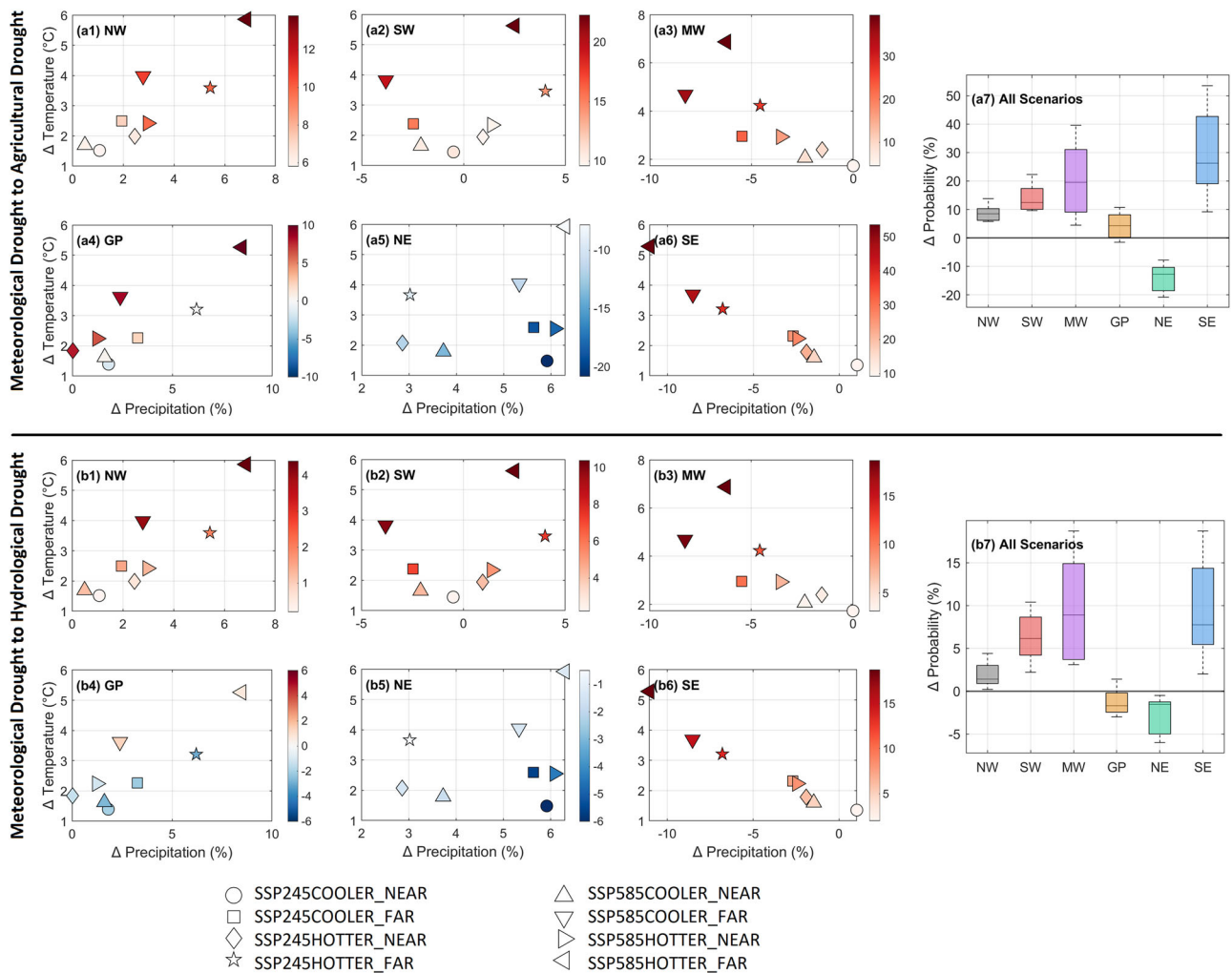


**Fig. 3 | Projected changes in drought propagation probabilities.** Scatterplot showing the projected changes in mean air temperature and mean annual precipitation under the eight scenarios, along with the percentage change in propagation probabilities. Barplot summarizing the regional differences in changing drought propagation probabilities across eight scenarios. **a** D1 meteorological drought

propagates to agricultural drought (including all D0–D4 events). **b** D1 meteorological drought propagates to hydrological drought (including all D0–D4 events). Note that different colormap scales are used for each subplot due to the significant differences in probability values among them.

exhibit stronger regional variations. As shown in Fig. 2, the MW and SE experience significant increases in total AD and HD duration and mean severity. Meanwhile, the NW, GP, and NE show either decreases or moderate increases in total duration due to rising annual precipitation, though mean severity still increases considerably under the SSP585HOTTER\_FAR scenario. In the NE region, only the SSP245COOLER\_NEAR scenario shows a decrease in mean severity. AD and HD also display distinct regional responses in annual frequency (Supplementary Figs. 10–15). In the NW and SW, the annual frequency of HD decreases while AD increases. The NE experiences declines in the annual frequency of both AD and HD, whereas the SE sees increases in both. The MW and GP show greater variability in the direction of change in AD and HD across the eight future scenarios, underscoring the complexity of drought propagation in these regions. For example, in the GP region, the annual frequency of AD increases moderately in three scenarios (SSP245COOLER\_NEAR, SSP245HOTTER\_NEAR, and SSP585HOTTER\_NEAR), decreases moderately in another three scenarios (SSP245COOLER\_FAR, SSP585COOLER\_NEAR, and SSP585HOTTER\_FAR), and shows no change in the remaining two scenarios (SSP245HOTTER\_FAR and SSP585COOLER\_FAR). Despite these regional differences, the mean severity of AD and HD is projected to rise across all regions (except for

a few scenarios in the NE), suggesting a higher likelihood of experiencing more severe AD and HD events across the CONUS, even as their occurrence frequency varies significantly.

### Shifting drought propagation probabilities

Under thermodynamic warming, the lag times between MD-AD and MD-HD events are projected to increase across all six regions (Supplementary Fig. 16), indicating that MD events will take longer to propagate into AD or HD events. This shift may be attributed to the projected increase in the duration of MD events (i.e., they start earlier and last longer). Consequently, a single MD event may trigger multiple AD or HD events, leading to extended lag times. Figure 3 illustrates the changes in drought propagation probabilities into AD and HD (including all categories D0–D4) following the occurrence of a D1 MD across all eight scenarios. We use D1 MD as an example because, under historical meteorological conditions, the mean MD intensity across all regions is D1, representing the expected historical baseline (Supplementary Table 6). However, the mean MD intensity is projected to increase in the future, reaching D2 or D3 in some regions.

Figure 3 shows that the MW and SE, which are projected to experience rising air temperatures and decreasing annual precipitation, exhibit the largest increases in drought propagation probabilities for both MD-AD and MD-HD. However, the magnitude of these increases varies by scenario, with

the highest probability increases occurring under the SSP585HOTTER\_FAR scenario. Specifically, under the SSP585HOTTER\_FAR scenario, the changes in MD-AD probabilities are 14%, 22%, 40%, 11%, -8%, and 54% for the NW, SW, MW, GP, NE, and SE, respectively, while under the SSP585HOTTER\_FAR scenario, the changes in MD-HD probabilities are 4%, 10%, 19%, 0.7%, -1%, and 19% for the same regions. It is interesting to observe that although the NW, GP, and NE are all projected to experience increased annual precipitation across all eight scenarios, their responses differ significantly. In the NE, consistent seasonal increases in precipitation and low precipitation seasonality lead to fewer AD and HD events throughout the year (Supplementary Table 6), reducing MD-AD and MD-HD propagation probabilities, even under the SSP585HOTTER\_FAR scenario. In contrast, the NW, characterized by high precipitation seasonality and most of the increase occurring during the cold season, experiences higher drought propagation probabilities for both MD-AD and MD-HD due to more frequent AD and HD conditions during the warm season. Similarly, the SW, which also has high precipitation seasonality like the NW, shows an increase in drought propagation probabilities despite inconsistent precipitation projections—half of the scenarios indicate increases, while the other half suggest decreases.

The GP region, however, presents a distinct response due to its relatively low precipitation seasonality and existing hydrological conditions. While annual precipitation increases moderately, summer precipitation declines, and air temperatures rise consistently across all seasons (Supplementary Figs. 2–5). These changes result in more frequent AD conditions during summer and fall, potentially increasing MD-AD propagation probabilities. However, several hydrological factors contribute to the decline in MD-HD propagation probabilities. First, the GP has the lowest runoff in the CONUS, and historical summer runoff in small CAMELS basins is already minimal. Since streamflow deficits define hydrological drought, the already low baseline runoff means that additional drying does not significantly exacerbate HD conditions—there is little runoff left to decline further. Second, while summer precipitation decreases, precipitation increases during other seasons help replenish soil moisture and sustain baseflow, mitigating prolonged hydrological drought conditions. Third, the region's low precipitation seasonality prevents extreme wet-dry shifts that would otherwise amplify MD-HD transitions. Collectively, these factors reduce the likelihood that an MD event progresses into an HD event, despite increased temperatures and seasonal drying. However, we acknowledge that drought propagation results in highly arid regions, such as the GP, can be particularly sensitive to the calibration of soil and surface runoff parameters due to the inherently low runoff conditions. This sensitivity represents one of the key limitations of our study. Uncertainty in CLM5 parameterization can significantly influence hydrological responses and contribute to variability in drought propagation outcomes. In this study, we employed a deterministic set of calibrated parameters chosen to best reproduce observed hydrologic behavior at each basin. However, we recognize the limitation of not explicitly quantifying the effects of parameter uncertainty on projected hydrologic changes, an important and active area of hydrologic modeling research. For instance, Yan et al.<sup>47</sup> demonstrated that uncertainty in CLM5 surface runoff and soil parameters plays a critical role in simulating low-flow conditions, with significant implications for drought-related decision-making. Eldardiry et al.<sup>38</sup> further emphasized that, when comparing meteorological forcing and CLM5 parametric uncertainty, the latter often dominates uncertainty in low-flow simulations. Building on this, Yan et al.<sup>42</sup> developed an ensemble-based, spatially distributed CLM5 parameter framework across CONUS and found that the large behavioral parameter space for low flows highlights the challenge of parameter equifinality in drought modeling. To date, the influence of CLM5 parameter uncertainty within the broader multi-model projection chain remains understudied, likely due to the substantial computational demands of large ensemble simulations. Future research should explicitly explore how parameter uncertainty affects hydrologic projections, particularly under warming scenarios.

Finally, we generated cumulative distribution functions (CDFs) for drought propagation, capturing each intensity category of AD and HD following an MD event across different intensities. Supplementary Figs. 17–26 present detailed probability values for each AD and HD intensity given D0–D4 MD events. Figure 4 illustrates the drought propagation CDFs for each intensity category of AD and HD following a D1 MD event. This intensity level was selected as an illustrative example because it represents the mean MD intensity under historical meteorological conditions across the CONUS. While the regional patterns resemble those in Fig. 3, Fig. 4 provides more specific insights into the probable drought intensities and their associated probabilities under eight future scenarios. In the NW, the probability of MD-AD propagation following a D1 MD event increases from 0.49 under historical conditions to 0.52–0.56 in future scenarios, representing a 5.8–13.8% increase. Conversely, in the NE, the probability of MD-AD given a D1 MD event decreases from 0.46 to 0.36–0.42, with reductions observed across nearly all drought intensity categories. The largest increase occurs in the SE, where the probability rises from 0.45 under historical conditions to as high as 0.69 under the SSP585HOTTER\_FAR scenario. However, when examining drought propagation across different intensity categories, notable variations emerge. Specifically, under the SSP585HOTTER\_FAR scenario, the probability of D0 AD declines, while probabilities for more intense drought categories (D2, D3, and D4 AD) increase across all regions. For other scenarios, however, regional variations exist. For instance, in the SP245COOLER\_NEAR scenario, the NE region shows a decrease in D2 probability. Nevertheless, the overall trend indicates a future shift toward more severe AD conditions, consistent with findings across other MD intensity categories (Fig. 1b, d).

For MD-HD propagation, Fig. 4 reveals generally higher probabilities compared to MD-AD. This reflects a stronger causal link between MD and HD compared to MD and AD. This finding is consistent with the literature<sup>59,60</sup>, showing that AD generally responds to MD more slowly and less frequently. This is because soil moisture deficits are influenced by the interplay of precipitation, evapotranspiration, soil properties, and antecedent moisture conditions, resulting in a more buffered and delayed response. Similar to MD-AD propagation, MD-HD propagation generally shows an increased likelihood of higher-intensity HD categories and a decreased likelihood of lower-intensity ones. However, exceptions exist in some regions. For instance, under the SSP585HOTTER\_FAR scenario, in the NW region, the probability of a D0 HD event following a D1 MD event decreases by 0.40%, while the probabilities of D2, D3, and D4 HD events increase by 11.2%, 14.0%, and 7.4%, respectively. In contrast, in the MW region, the probability of a D0 HD event following a D1 MD event decreases by 7.0%, but the D4 HD probability also declines by 23.7%. This is likely because relatively few D1 MD events in the MW have led to extreme HD intensities, limiting the frequency of such transitions. However, as the initiating MD events intensify, the propagation patterns between MD-AD and MD-HD become more aligned, with a more proportional likelihood of higher intensity. Notably, under SSP585HOTTER\_FAR in the MW, the probability of a D3 HD event following a D3 MD event is projected to increase by 75.4%, while the probability of a D4 HD event rises by 31.7%. Given that future MD intensities are projected to be higher—shifting from D1 toward D2 and D3 in some regions—these findings suggest that MD-HD propagation will also result in more persistent and severe HD conditions in the future.

In summary, our results reveal considerable regional variations in drought propagation probabilities across the CONUS, highlighting the complex interplay between temperature, precipitation, seasonality, and drought intensity. Understanding these regional patterns in drought propagation probabilities is essential for informing risk management strategies. While rising temperatures are projected to intensify MD across all regions, their effects on AD and HD propagation differ. For example, the MW and SE show the largest increases in MD-AD and MD-HD propagation probabilities, driven by warming temperatures and declining precipitation. In contrast, regions with distinct precipitation seasonality—such as the NE, where precipitation increases consistently across all seasons, and the NW,

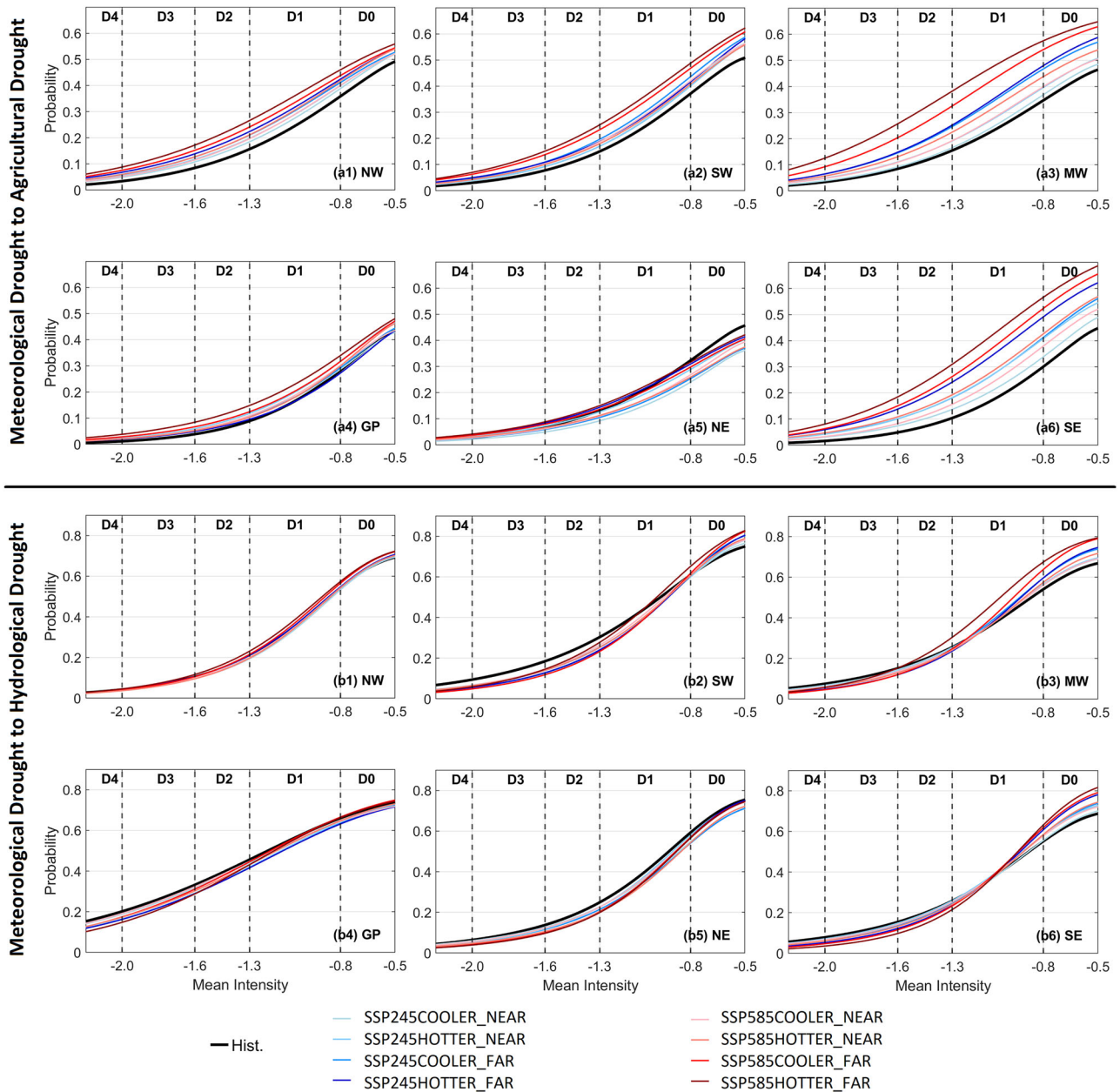


**Fig. 4 | Propagation probabilities following the occurrence of a D1 meteorological drought. a** Meteorological drought to agricultural drought (AD). **b** Meteorological drought to hydrological drought (HD). The nine cumulative distribution functions (CDFs) represent the historical scenario and eight future

projection scenarios. The probability of each AD/HD intensity level—from D0 to D4—can be estimated by calculating the difference between corresponding points on the CDFs.

where increases are concentrated primarily in the cold season—exhibit more complex propagation patterns, emphasizing the importance of local meteorological factors in shaping drought risks. These regional variations have significant implications for both water management and agriculture. The MW and SE, which include key agricultural regions in the U.S., face heightened risks of crop failure and water shortages due to increased drought propagation. This calls for targeted drought management strategies, such as improved water resource management, development of drought-resistant crops, and adaptive agricultural practices to enhance resilience in these crucial food-producing areas. Conversely, regions such as the NE, where precipitation is more consistent year-round, show reduced drought propagation probabilities, suggesting greater resilience to the impacts of thermodynamic change.

Thermodynamic change alters drought propagation dynamics, with significant implications for both natural ecosystems and human-managed environments. The increasing likelihood of MD triggering more severe AD and HD necessitates a deeper understanding of their cascading effects, particularly in regions prone to compound extreme events. These drought propagation CDFs offer useful insights for technology transition and risk assessment. Understanding these probabilities allows stakeholders to anticipate potential drought impacts and incorporate them into decision-making frameworks, such as cost-loss models, where the benefits of early intervention can be weighed against the risks and costs of inaction. In particular, the increasing likelihood of drought propagation highlights the need for enhanced early warning systems and proactive adaptation strategies to mitigate future drought risks. Seasonal to sub-seasonal drought early warning systems are essential for proactive drought management, providing

water resource managers, farmers, and policymakers with critical lead time to implement adaptive strategies and mitigate potential impacts. Our findings, particularly the increased probabilities of MD propagating into AD and HD, as well as the trend toward higher-intensity drought outcomes, highlight important changes in the future drought risk landscape. Furthermore, the projected increase in lag time between the onset of MD and the development of AD and HD impacts underscores the need for extended forecasting horizons and the development of region-specific risk indicators that account for evolving propagation dynamics and intensities. For example, in the GP, the mean lag time between MD and AD increases from 1.4 months under the historical climate to 3.4 months under the SSP585HOTTER\_FAR scenario.

It is important to note that this study uses the six-region classification of CONUS based on Xia et al.<sup>58</sup> to aggregate basins for probabilistic analysis. While this framework provides a reasonable basis for regionalization, it inevitably groups together basins with distinct hydroclimatic characteristics. For example, the MW region includes both humid eastern areas and more arid or semi-arid western areas commonly associated with the North Great Plains. Aggregating basins across diverse hydroclimatic zones may obscure important sub-regional differences in drought propagation dynamics. As shown in Fig. 2, heterogeneous patterns in drought characteristics such as duration and severity are evident within each region. Therefore, the regional results presented here should be interpreted as average headwater basin conditions and responses, which may underrepresent localized vulnerabilities or more complex sub-regional behaviors. To better capture these sub-regional differences, future studies could consider adopting finer-scale regional classifications for analysis.

In this study, we specifically chose SPEI to represent MD because it accounts for temperature-driven changes in atmospheric moisture demand (via PET), which aligns with our focus on thermodynamic warming impacts on drought propagation. For comparison, we also used the Standardized Precipitation Index (SPI) index to characterize MD, and the results versus MD using the SPEI index are shown in Supplementary Fig. 9. The comparison between SPEI and SPI results highlights the critical role of temperature in aggravating future MD conditions. Both MD total duration and mean severity show substantial increases when using SPEI compared to SPI. For example, under the SSP245COOLER\_NEAR scenario, the increase in annual precipitation in the NE region leads to a decrease in MD total duration and mean severity in most basins when using SPI, while SPEI shows an increase in both metrics in the same basins. However, SPI alone may fail to identify MD events in regions where temperature increases significantly alter moisture demand. For instance, in basin 11124500 near Santa Barbara, CA, during June 2016, a record-breaking heatwave occurred, Burbank reached 44 °C, severely impacting local agriculture. Precipitation for that month is generally zero, resulting in an SPI-1 of -0.03 (normal), while the SPEI-1 was -1.85 (D3 MD), more accurately capturing the drought stress. This reflects a common issue in the western U.S., where summers typically receive little precipitation, and high-temperature-driven droughts may be misrepresented, or entirely missed, when using SPI alone. Consequently, using SPI can underestimate MD intensity during drought propagation, potentially causing a mismatch where less severe MD events appear to trigger more severe AD or HD events. This can bias results, especially since AD and HD are also influenced by vapor pressure deficit. The importance of including temperature in MD characterization has also been emphasized in previous studies<sup>8,61,62</sup>, which show that indices excluding temperature can underestimate drought intensity and impacts, especially under warming conditions. While the Palmer Drought Severity Index (PDSI) is also widely used to characterize MD events, we chose not to use it in this study due to its limitations across diverse climatic and geographic regions. PDSI is highly sensitive to calibration parameters and local soil characteristics, which undermines its reliability for spatial comparisons across basins with differing hydrological conditions<sup>63,64</sup>. In contrast, standardized drought indices such as SPEI and SPI have been recommended by the World Meteorological Organization as key drought indicators due to their transparency and extendibility for multi-scalar analysis<sup>65</sup>.

Lastly, a limitation of this study is the use of root-zone soil moisture to represent agricultural drought, which does not capture plant physiological responses under rising CO<sub>2</sub>. While root-zone soil moisture is a useful hydrological indicator, it does not differentiate between plant functional types or account for CO<sub>2</sub>-driven changes in additional vegetation growth and stomatal behavior<sup>66,67</sup>. Alternative vegetation-based metrics, such as Gross Primary Productivity, may better represent plant stress due to water availability<sup>68,69</sup>. Moreover, this study uses CLM5 in Satellite Phenology (SP) mode, which relies on satellite-derived phenology and is computationally efficient but does not simulate dynamic vegetation or CO<sub>2</sub> fertilization effects. Future research should explore the implications of rising CO<sub>2</sub> and plant physiological feedbacks using models such as CLM5-Biogeochemistry, which explicitly represent these processes and can improve understanding of agricultural drought risk, particularly in terms of crop yield and productivity. Due to the limited availability of in-situ root-zone soil moisture data and the constraint that satellite products primarily provide surface soil moisture, estimating the full drought propagation chain, especially MD to AD, requires model-based approaches. This study used observed streamflow to calibrate the CLM5 model for each basin, improving the model's ability to replicate historical hydrologic processes and increasing confidence in its projections of future drought propagation. Nonetheless, we acknowledge that direct observations provide a more robust understanding of historical drought propagation, particularly the transition from MD to HD, and that these may differ slightly from model-based estimates. Future studies could benefit from incorporating hydrologic data assimilation techniques<sup>31,70-74</sup> to improve the reconstruction of historical root-zone soil moisture and enhance our understanding of drought development. Additionally, remote sensing indicators such as vegetation optical depth from microwave sensors can complement model estimates by providing spatially continuous insights into vegetation responses to drought<sup>8</sup>.

## Methods

### Study basins

The CAMELS data sets<sup>48,49</sup> build upon the previous Model Parameter Estimation Experiment (MOPEX) data sets<sup>75</sup> by incorporating 671 headwater basins with minimal human influence across the CONUS. These data sets provide high-quality, unregulated daily streamflow measurements for each basin from 1980 to 2014. Additionally, they include basin area information derived from two independent sources: the national geospatial fabric polygon<sup>76</sup> and the United States Geological Survey Geospatial Attributes of Gages for Evaluating Streamflow version II database<sup>77</sup>. For this study, we selected 464 basins where the difference in basin area estimates from the two sources was less than 2%, following the recommendation of Addor et al.<sup>48</sup>. This criterion ensures consistency in basin delineation, which is critical for accurate hydrological modeling. The spatial distribution of these selected basins (Fig. 2) captures the diverse hydroclimatic gradients of the CONUS, spanning regions such as the Pacific Northwest, Northeast, Great Plains, and more. The selected basins vary widely in size, ranging from approximately 4 km<sup>2</sup> to 25,791 km<sup>2</sup>, with a median area of 436 km<sup>2</sup>. Their mean elevations also exhibit significant variability, from as low as 15 m in the Delaware region to as high as 3529 m in the Southern Rocky Mountains, with a median elevation of 458 m. This broad range in physiographic characteristics ensures that our study encompasses a representative sample of the diverse hydrological conditions across the CONUS.

### Dataset

The TGW dataset provides dynamically downscaled meteorological projections for the CONUS, covering a 40-year historical period (1980–2019) and two 40-year future periods: NEAR future (2020–2059) and FAR future (2060–2099). These future projections are based on simulations driven by two CMIP6 greenhouse gas emissions scenarios: SSP245, which represents a stabilization pathway with moderate mitigation efforts, and SSP585, a high-emissions scenario characterized by continued fossil fuel use and minimal climate mitigation. For the historical period, the WRF model (version 4.2.1)<sup>78</sup> was used to dynamically downscale the ERA5 reanalysis dataset<sup>44</sup> to

a spatial resolution of  $1/8^\circ$  ( $\sim 12$  km). For the future projections, the TGW simulations employ the perturbed thermodynamics experiments, which modify historical weather patterns based on projected thermodynamics changes such as temperature and humidity derived from a multi-model ensemble of CMIP6 GCMs. This approach preserves the dynamical consistency of past weather while simulating how extreme events may shift under perturbed thermodynamics.

In the TGW framework described by Jones et al.<sup>43</sup>, CMIP6 models are selected based on several key criteria to ensure robust and representative thermodynamic signals. The selection process is based on three main criteria: model performance over the CONUS, availability of required variables, and institutional independence. Models are first filtered to include only those ranked among the top 25 in a comprehensive performance assessment. From this subset, only those providing all necessary monthly variables—air temperature, near-surface air temperature, skin temperature, relative humidity, and sea surface temperature—for both SSP245 and SSP585 scenarios are retained. Depending on data availability, one to five ensemble members are used per model. To maintain model independence and avoid over-representation of structurally similar models, only one model per institution is included. The final set consists of NorESM2-MM, GISS-E2-1-G, GFDL-ESM4, ACCESS-ESM1-5, CNRM-CM6-1-HR, UKESM1-0-LL, HadGEM3-GC31-LL, and CanESM5. These models are further grouped into high- (HOTTER) and low-sensitivity (COOLER) categories based on projected changes in CONUS mean temperature under SSP585. Thermodynamic change signals are calculated using monthly GCM data, and ensemble means are computed separately for the high- and low-sensitivity groups.

The TGW dataset provides high-resolution climate data, including 25 hourly variables and over 200 three-hourly variables at 12 km spatial resolution across CONUS. Key variables include temperature, precipitation, humidity, wind speed, and radiation, among others, supporting a wide range of hydrological and atmospheric research applications. A significant advantage of this dataset is its ability to assess how specific historical climate events might evolve under future thermodynamic warming, making it a useful tool for extreme event impact assessment and adaptation planning. For a detailed description of TGW and its implementation, see Jones et al.<sup>43</sup>. Validation of the historical TGW simulations against observational data is provided in Srivastava et al.<sup>79</sup>. Their findings indicate that TGW performs comparably to ERA5 in capturing the timing and magnitude of the diurnal precipitation peak across most of CONUS. Additionally, TGW significantly improves the accuracy of both the timing and magnitude of the annual cycle of monthly mean precipitation compared to ERA5.

### CLM5 configuration and calibration

The structure of the CLM5 model has been comprehensively detailed in previous studies<sup>45,80</sup>, so we do not reiterate it here. In this study, we employ the recently developed CLM5-Perturbed Parameter Ensembles (PPE) version<sup>81,82</sup> to conduct land surface simulations, which allows users to perturb the default hard-coded parameters within CLM5. CLM5-PPE is configured for each CAMELS basin and land surface data input such as land type and plant functional types are acquired from the CLM5 default configuration at a  $1/8^\circ$  grid cell resolution across the CONUS<sup>45</sup>. At these same CAMELS basins, Yan et al.<sup>46,47</sup> conducted an extensive diagnostic evaluation of CLM5 hydrological parameter uncertainty, analyzing large ensemble simulations for 15 hydrological parameters that encompass a wide range of hydrological processes, including canopy water, surface water, soil water, subsurface water, snow, and evaporation. Their findings suggest that the default CLM5 hydrological parameters lead to poor to moderate runoff predictions, particularly in arid regions, underscoring the need for model calibration in hydrological applications. In the model calibration, we use the Latin Hypercube Sampling method to sample 1500 hydrological parameter sets from their uniform prior distributions, as identified by Yan et al.<sup>47</sup>, resulting in a total of  $1500 \times 464 = 696,000$  CLM5 runs. We then select the hydrological parameter set that yields the highest KGE<sup>57</sup> for each basin. The KGE is a weighted metric that assesses model performance in terms of

correlation, mean bias, and variability bias and is widely used in drought applications<sup>53,83,84</sup>. The KGE ranges from  $-\infty$  to 1, with a value of 1 indicating a perfect match between observations and simulations. As suggested by Dagon et al.<sup>81</sup>, each CLM5 simulation is spun up for 15 years to equilibrate all state variables. Both historical and future simulations use the same initial conditions to maintain consistency.

We acknowledge that the Noah LSM is coupled with WRF and provides land surface variables for downscaling. However, Noah LSM is not calibrated or validated for hydrologic predictions in our study basins. Our WRF setup is intended primarily to provide downscaled climate forcing rather than accurate hydrological simulations. The lack of calibration can lead to considerable biases in historical drought simulations that propagate into future projections, as pointed out in previous studies<sup>33–35</sup>. Compared to Noah, CLM5 offers a more comprehensive and physically based representation of hydrological processes<sup>85</sup>. However, Yan et al.<sup>47</sup> demonstrated that using default parameters in CLM5 can still lead to substantial biases in streamflow simulations, particularly in arid regions. In this study, we address this challenge by coupling WRF outputs with individually calibrated CLM5 models for each CAMELS basin using resources at DOE-NERSC (U.S. Department of Energy's National Energy Research Scientific Computing Center). The calibrated CLM5 models significantly improve streamflow simulation (Supplementary Fig. 1), enhancing both the representation of historical hydrological processes and the credibility of future drought projections. Nonetheless, this approach does not account for land-atmosphere feedbacks, which may influence drought dynamics in certain regions and warrant further investigation.

### Drought characterization

We use the Standardized Precipitation Evapotranspiration Index (SPEI)<sup>50</sup> to characterize meteorological drought, calculated from the difference between precipitation and potential evapotranspiration (PET). Unlike the Standardized Precipitation Index (SPI)<sup>86</sup>, SPEI accounts for the balance between water input (precipitation) and water loss (PET), offering a more precise measure of moisture availability compared to SPI. This distinction is particularly significant in regions where increasing temperatures could elevate evapotranspiration rates, exacerbating drought conditions even if precipitation remains unchanged, as observed during summer in the western U.S.<sup>61,87–89</sup>. The hourly PET data are calculated using the Penman–Monteith method<sup>90</sup> based on the TGW. To characterize agricultural and hydrological droughts, we use the Standardized Soil Moisture Index (SSMI)<sup>51</sup> and the Standardized Runoff Index (SRI)<sup>52</sup>, respectively. These indices are derived using root-zone soil moisture ( $<1$  m) and total runoff simulated by CLM5. SPEI, SSMI, and SRI are calculated similarly by fitting a selected distribution to the data for each month, computing the CDF, and transforming it using the inverse of the standard normal distribution. Following the approach used for SPI to address zero precipitation values<sup>91</sup>, zero runoff values in the SRI calculation were explicitly treated using a mixed distribution  $H(z)$ :

$$H(z) = q + (1 - q)G(z) \quad (1)$$

where  $q$  is the probability of zero runoff and  $G(z)$  is the CDF of the fitted distribution for  $z > 0$ . To address near-zero runoff values produced by numerical artifacts in CLM5, monthly runoff values less than 0.01 mm were set to zero prior to SRI calculation.

Using the L-moment ratio diagram method<sup>92,93</sup>, we identify the generalized logistic (GLO), generalized Pareto, and Pearson Type III distributions as the best-fit among 11 candidate probability density functions (PDFs) (see Supplementary Table 18) for SPEI, SSMI, and SRI, respectively, across most basins in the CONUS. These distributions are therefore employed in this study. Note that the PDF parameters are derived from the historical period simulation, and the same PDFs are applied to all eight future simulations. Although both single-month and multi-timescale standardized indices (e.g., 3-, 6-, and 12-month) can be used to define drought events, multi-timescale indices often introduce significant information overlap (e.g., SPEI-3 for April includes data from February, March,

and April, which partially overlaps with SPEI-3 for May), potentially inflating drought duration and severity in propagation analysis. To avoid this, we employ 1-month SPEI, SSMI, and SRI indices to characterize the dry and wet states. While this approach effectively captures the timing and propagation of drought events, consistent with prior studies<sup>16,94,95</sup>, it may not fully capture flash droughts, which evolve on a weekly scale<sup>96</sup>. These rapid-onset events, often driven by a combination of high evaporative demand and precipitation deficits, can intensify quickly and severely impact agricultural systems before standard drought indices detect them. Recent research has identified flash droughts as a critical mechanism of AD intensification under rising temperatures<sup>13,97</sup>. Consequently, the use of a 1-month timescale in this study, while appropriate for characterizing broader drought evolution, may underestimate future AD risk by missing these short-lived but high-impact events. This suggests our results may represent a conservative estimate of future drought-related agricultural vulnerability.

After calculating the SPEI, SSMI, and SRI, we apply run theory<sup>98</sup> to extract drought events from the three drought index series (Fig. 1a). Drought intensity is classified into five categories based on the U.S. Drought Monitor (USDM)<sup>3</sup>: D0 (abnormally dry,  $\leq -0.5$ ), D1 (moderate drought,  $\leq -0.8$ ), D2 (severe drought,  $\leq -1.3$ ), D3 (extreme drought,  $\leq -1.6$ ), and D4 (exceptional drought,  $\leq -2.0$ ). To minimize the impact of minor, potentially interdependent droughts on our analysis, drought events with intervals of less than 3 months between their end and onset are merged into a single event<sup>13,99</sup>. Figure 1a illustrates that drought event duration is the total period from onset to end, severity is the sum of index values for months with SPEI/SSMI/SRI  $\leq -0.5$ , and intensity is the severity divided by duration. The next step involves matching MD-AD and MD-HD drought propagation events. If an AD/HD onset occurs within the duration of an MD, the MD is considered to have triggered the AD/HD, and the lag time is calculated as the difference in the timing of their occurrences (Fig. 1a). Multiple MDs may precede or coincide with an AD/HD, and multiple AD/HDs may occur during a single MD. These cases are also considered matched drought events<sup>16,100</sup>. Given the basin's inherent regulatory capabilities, not all MDs will trigger AD/HDs.

### Probabilistic drought propagation model

The propagation model uses Bayesian networks to capture the conditional dependencies between matched MD-AD and MD-HD events. The core of this propagation model is to predict the distribution of AD/HD following a specific MD intensity (Fig. 1c). Due to the limited number of matched events in each individual basin, we employ regional analysis to compensate for the sparse data by pooling matched drought events from all basins within each region. Consequently, each region across the CONUS has its own propagation model. To estimate the joint distribution between MD and AD/HD, we use a copula function<sup>101,102</sup>, which is a multivariate distribution function for uniformly distributed variables over the interval [0, 1]. While the mathematical properties of copula functions are well-documented<sup>54,103,104</sup>, we provide a brief overview here. In the following, we use MD-AD as an example, and a similar procedure is applied to MD-HD.

Let  $X$  represent the MD intensities and  $Y$  represent the AD intensities. According to Sklar's theorem<sup>105</sup>, a bivariate distribution can be expressed using a copula function as follows:

$$F_{X,Y}(x,y) = C[F_X(x), F_Y(y)] \quad (2)$$

where  $C$  is the CDF of copula,  $F_X(x)$  and  $F_Y(y)$  are the marginal CDFs of  $X$  and  $Y$ . The conditional PDF  $f_{Y|X}(y|x)$  is then derived as:

$$f_{Y|X}(y|x) = c[F_X(x), F_Y(y)] \cdot f_Y(y) \quad (3)$$

where  $c$  is the PDF of the copula function and  $f_Y(y)$  is the PDF of marginal distribution for AD intensities. As shown in Fig. 2c, once the conditional PDF for a specific MD drought intensity (e.g., D1) is obtained from Eq. (2), the probability that the AD intensity is less than a threshold, i.e.,  $F_{Y|X}(Y < y|X = x)$ , is computed as the area under  $f_{Y|X}(y|x)$  for  $Y < y$ .

Among various copula families, the Archimedean and elliptical families are commonly used in drought applications<sup>106</sup>. In this study, we consider Gaussian and t copulas from the elliptical family, and Clayton and Frank copulas from the Archimedean family. Based on the parametric bootstrapping goodness-of-fit test<sup>107,108</sup>, the Frank copula provides the best fit for most regions for both MD-AD and MD-HD events and is selected for this study.

However, it is important to note that the conditional PDF is modeled based only on the matched MD-AD events, rather than on all MD events, since not all MD events will necessarily lead to AD. This limitation can lead to an overestimation of drought propagation probabilities. To address this, we use the Law of Total Probability to incorporate the propagation rate term, which is defined as the percentage of MDs that trigger AD/HDs relative to the total number of MDs<sup>7</sup>. Let  $S$  denote that MD leads to AD, and  $F$  denote that MD does not lead to AD. The probabilities  $P(Y|X)$  can be expressed as<sup>109</sup>:

$$P(Y|X) = P(Y|X, S) \cdot P(S|X) + P(Y|X, F) \cdot P(F|X) \quad (4)$$

where  $P(S|X)$  is the MD-AD propagation rate, and  $P(Y|X, S)$  is modeled using Eq. (3). Since we focus on the MD-AD,  $P(Y|X, F) = 0$ . Thus, Eq. (4) simplifies to:

$$P(Y|X) = P(Y|X, S) \cdot P(S|X) \quad (5)$$

In our study, we used the same copula function to model both historical and future conditional probability distributions to ensure consistency in the relative comparison. However, we acknowledge that using multiple copula families, or selecting the best-fit copula function for each region individually, could potentially better represent uncertainty in drought propagation. For example, elliptical copulas such as the t copula are known to better capture tail dependence compared to other families. To assess the sensitivity of our results to copula choice, we conducted a sensitivity test by replacing the Frank copula with the t copula in modeling drought propagation. Results suggest that while absolute probabilities may vary slightly with copula choice, the key patterns of change remain consistent. For instance, under the SSP585HOTTER\_FAR scenario in the MW region, given the occurrence of D1 MD, the probability of subsequent D0 AD decreased by 40% (from 0.12 to 0.07) using the Frank copula, and by 38% (from 0.13 to 0.08) using the t copula. Similarly, the probability of propagating to D3 AD increased by 163% (from 0.05 to 0.13) and 158% (from 0.05 to 0.12) using the Frank and t copulas, respectively. This aligns with findings from Peng et al.<sup>110</sup>, demonstrating that the sensitivity to copula selection diminishes as the sample size increases. A similar limitation arises from the application of a single marginal distribution across regions in drought characterization. In this study, we used the GLO distribution for SPEI across all regions. However, the Generalized Extreme Value distribution, with its heavier tails, may be more appropriate for capturing extreme drought events. Despite these considerations, prior studies suggest that the impact of selecting different copula functions or marginal distributions is relatively small compared to other sources of uncertainty. For instance, Yan and Moradkhani<sup>111</sup> found that, when compared to the influence of model structure, the choice of statistical distribution played a considerably smaller role in flood uncertainty quantification.

### Data availability

The TGW climate data are available at <https://tgw-data.msdlive.org/>. The CAMELS data set is available at <https://ral.ucar.edu/solutions/products/camels>. This experiment used a modified version of CLM5 designed to allow easier parameterization and support machine-specific compilation. The modified source code is available at <https://doi.org/10.5281/zenodo.6653704>, forked from [https://github.com/ESCOMP/CTSM/tree/branch\\_tags/PPE.n11\\_ctsm5.1.dev030](https://github.com/ESCOMP/CTSM/tree/branch_tags/PPE.n11_ctsm5.1.dev030). The calibrated CLM5 hydrological data are available at <https://doi.org/10.57931/1922953>. Links to all supporting

software and data sets for this paper, along with instructions for reproducing the analysis, are available at <https://doi.org/10.5281/zenodo.15692289>.

Received: 17 March 2025; Accepted: 24 July 2025;  
Published online: 03 October 2025

## References

- AghaKouchak, A. et al. Toward impact-based monitoring of drought and its cascading hazards. *Nat. Rev. Earth Environ.* **4**, 582–595 (2023).
- Mishra, A. K. & Singh, V. P. A review of drought concepts. *J. Hydrol.* **391**, 202–216 (2010).
- Svoboda, M. et al. The drought monitor. *Bull. Am. Meteorol. Soc.* **83**, 1181–1190 (2002).
- Ahmadalipour, A., Moradkhani, H., Yan, H. & Zarekarizi, M. Remote sensing of drought: vegetation, soil moisture, and data assimilation. *Remote Sensing of Hydrological Extremes* (ed. Lakshmi, V.) 121–149. [https://doi.org/10.1007/978-3-319-43744-6\\_7](https://doi.org/10.1007/978-3-319-43744-6_7) (Springer International Publishing Switzerland, 2017).
- Wilhite, D. A. & Glantz, M. H. Understanding: the drought phenomenon: the role of definitions. *Water Int.* **10**, 111–120 (1985).
- Chagnon, S. *Detecting Drought Conditions in Illinois. Illinois State Water Survey Champaign Circular 169* (1987).
- Zhang, X. et al. Drought propagation under global warming: characteristics, approaches, processes, and controlling factors. *Sci. Total Environ.* **838**, 156021 (2022).
- Entekhabi, D. Propagation in the drought cascade: observational analysis over the continental US. *Water Resour. Res.* **59**, e2022WR032608 (2023).
- Apurv, T., Sivapalan, M. & Cai, X. Understanding the role of climate characteristics in drought propagation. *Water Resour. Res.* **53**, 9304–9329 (2017).
- Gevaert, A. I., Veldkamp, T. I. E. & Ward, P. J. The effect of climate type on timescales of drought propagation in an ensemble of global hydrological models. *Hydrol. Earth Syst. Sci.* **22**, 4649–4665 (2018).
- Barker, L. J., Hannaford, J., Chiveron, A. & Svensson, C. From meteorological to hydrological drought using standardised indicators. *Hydrol. Earth Syst. Sci.* **20**, 2483–2505 (2016).
- Han, Z. et al. Propagation dynamics from meteorological to groundwater drought and their possible influence factors. *J. Hydrol.* **578**, 124102 (2019).
- Yang, X. et al. Quantifying the impact of human activities on hydrological drought and drought propagation in China using the PCR-GLOBWB v2.0 model. *Water Resour. Res.* **60**, e2023WR035443 (2024).
- Yang, X. et al. Contrasting influences of human activities on hydrological drought regimes over China based on high-resolution simulations. *Water Resour. Res.* **56**, e2019WR025843 (2020).
- AghaKouchak, A. et al. Anthropogenic drought: definition, challenges, and opportunities. *Rev. Geophys.* **59**, e2019RG000683 (2021).
- Guo, Y. et al. Propagation thresholds of meteorological drought for triggering hydrological drought at various levels. *Sci. Total Environ.* **712**, 136502 (2020).
- Yao, L., Ferencz, S. B., Sun, N. & Yan, H. Assessing the complex influences of water management on hydrological drought characteristics in Texas. *Environ. Res. Lett.* **19**, 114034 (2024).
- Kumar, S. V., Harrison, K. W., Peters-Lidard, C. D. & Santanello, J. A. & Kirschbaum, D. Assessing the impact of L-band observations on drought and flood risk estimation: a decision-theoretic approach in an OSSE environment. *J. Hydrometeorol.* **15**, 2140–2156 (2014).
- Portele, T. C. et al. Seasonal forecasts offer economic benefit for hydrological decision-making in semi-arid regions. *Sci. Rep.* **11**, 10581 (2021).
- Madadgar, S., AghaKouchak, A., Farahmand, A. & Davis, S. J. Probabilistic estimates of drought impacts on agricultural production. *Geophys. Res. Lett.* **44**, 7799–7807 (2017).
- Yan, H., Zarekarizi, M. & Moradkhani, H. Toward improving drought monitoring using the remotely sensed soil moisture assimilation: a parallel particle filtering framework. *Remote Sens. Environ.* **216**, 456–471 (2018).
- IPCC. *Climate Change 2013: The Physical Science Basis. Contribution of Working Group I to the Fifth Assessment Report of the Intergovernmental Panel on Climate Change.* <https://doi.org/10.1017/CBO9781107415324> (Cambridge University Press, 2013).
- Mukherjee, S., Mishra, A. & Trenberth, K. E. Climate Change and drought: a perspective on drought indices. *Curr. Clim. Chang. Rep.* **4**, 145–163 (2018).
- Yan, H., Sun, N., Fullerton, A. & Baerwalde, M. Greater vulnerability of snowmelt-fed river thermal regimes to a warming climate. *Environ. Res. Lett.* **16**, 054006 (2021).
- Kreibich, H. et al. The challenge of unprecedented floods and droughts in risk management. *Nature* **608**, 80–86 (2022).
- Ullah, I. et al. Anthropogenic and atmospheric variability intensifies flash drought episodes in South Asia. *Commun. Earth Environ.* **5**, 267 (2024).
- Vicente-Serrano, S. M. et al. Evidence of increasing drought severity caused by temperature rise in southern Europe. *Environ. Res. Lett.* **9**, 044001 (2014).
- Leng, G., Tang, Q. & Rayburg, S. Climate change impacts on meteorological, agricultural and hydrological droughts in China. *Glob. Planet. Change* **126**, 23–34 (2015).
- Jehanzaib, M., Sattar, M. N., Lee, J.-H. & Kim, T.-W. Investigating effect of climate change on drought propagation from meteorological to hydrological drought using multi-model ensemble projections. *Stoch. Environ. Res. Risk Assess.* **34**, 7–21 (2020).
- Strzepek, K., Yohe, G., Neumann, J. & Boehlert, B. Characterizing changes in drought risk for the United States from climate change. *Environ. Res. Lett.* **5**, 044012 (2010).
- Zhou, Z. et al. Insights from CMIP6 SSP scenarios for future characteristics of propagation from meteorological drought to hydrological drought in the Pearl River Basin. *Sci. Total Environ.* **899**, 165618 (2023).
- Mendoza, P. A. et al. Are we unnecessarily constraining the agility of complex process-based models?. *Water Resour. Res.* **51**, 716–728 (2015).
- Su, L., Lettenmaier, D. P., Pan, M. & Bass, B. Improving runoff simulation in the Western United States with Noah-MP and variable infiltration capacity. *Hydrol. Earth Syst. Sci.* **28**, 3079–3097 (2024).
- Chaney, N. W., Herman, J. D., Reed, P. M. & Wood, E. F. Flood and drought hydrologic monitoring: the role of model parameter uncertainty. *Hydrol. Earth Syst. Sci.* **19**, 3239–3251 (2015).
- Cheng, Y. et al. Moving land models toward more actionable science: a novel application of the community terrestrial systems model across Alaska and the Yukon River Basin. *Water Resour. Res.* **59**, e2022WR032204 (2023).
- Cheng, Y. et al. Coupled high-resolution land-atmosphere modeling for hydroclimate and terrestrial hydrology in Alaska and the Yukon River Basin (1990–2021). *J. Geophys. Res. Atmos.* **130**, e2024JD041185 (2025).
- Blaskey, D. et al. A high-resolution, daily hindcast (1990–2021) of Alaskan river discharge and temperature from coupled and optimized physical models. *Water Resour. Res.* **60**, e2023WR036217 (2024).
- Eldardiry, H. et al. Characterizing how meteorological forcing selection and parameter uncertainty influence community land model version 5 hydrological applications in the United States. *J. Adv. Model. Earth Syst.* **17**, e2024MS004222 (2025).

39. Hejazi, M. I. et al. 21st century United States emissions mitigation could increase water stress more than the climate change it is mitigating. *Proc. Natl. Acad. Sci.* **112**, 10635–10640 (2015).
40. Cheng, Y. et al. Future bioenergy expansion could alter carbon sequestration potential and exacerbate water stress in the United States. *Sci. Adv.* **8**, (2022).
41. Yuan, X. et al. A global transition to flash droughts under climate change. *Science* **380**, 187–191 (2023).
42. Yan, H. et al. Ensemble-based spatially distributed CLM5 hydrological parameter estimation for the continental United States. *J. Adv. Model. Earth Syst.* **17**, e2024MS004227 (2025).
43. Jones, A. D. et al. Continental United States climate projections based on thermodynamic modification of historical weather. *Sci. Data* **10**, 664 (2023).
44. Hersbach, H. et al. The ERA5 global reanalysis. *Q. J. R. Meteorol. Soc.* **146**, 1999–2049 (2020).
45. Lawrence, D. et al. The community land model version 5: description of new features, benchmarking, and impact of forcing uncertainty. *J. Adv. Model. Earth Syst.* **11**, 4245–4287 (2019).
46. Yan, H. et al. Characterizing uncertainty in Community Land Model version 5 hydrological applications in the United States. *Sci. Data* **10**, 187 (2023).
47. Yan, H. et al. Large ensemble diagnostic evaluation of hydrologic parameter uncertainty in the Community Land Model Version 5 (CLM5). *J. Adv. Model. Earth Syst.* **15**, e2022MS003312 (2023).
48. Addor, N., Newman, A. J., Mizukami, N. & Clark, M. P. The CAMELS data set: catchment attributes and meteorology for large-sample studies. *Hydrol. Earth Syst. Sci.* **21**, 5293–5313 (2017).
49. Newman, A. J. et al. Development of a large-sample watershed-scale hydrometeorological data set for the contiguous USA: data set characteristics and assessment of regional variability in hydrologic model performance. *Hydrol. Earth Syst. Sci.* **19**, 209–223 (2015).
50. Vicente-Serrano, S. M., Beguería, S. & López-Moreno, J. I. A multiscalar drought index sensitive to global warming: the standardized precipitation evapotranspiration index. *J. Clim.* **23**, 1696–1718 (2010).
51. Hao, Z. & AghaKouchak, A. A Nonparametric multivariate multi-index drought monitoring framework. *J. Hydrometeorol.* **15**, 89–101 (2014).
52. Shukla, S. & Wood, A. W. Use of a standardized runoff index for characterizing hydrologic drought. *Geophys. Res. Lett.* **35**, (2008).
53. Yan, H., Moradkhani, H. & Zarekarizi, M. A probabilistic drought forecasting framework: a combined dynamical and statistical approach. *J. Hydrol.* **548**, 291–304 (2017).
54. Zarekarizi, M., Yan, H., Ahmadalipour, A. & Moradkhani, H. A probabilistic framework for agricultural drought forecasting using the ensemble data assimilation and Bayesian multivariate modeling. *Global Drought and Flood: Observation, Modeling, and Prediction* 147–164. <https://doi.org/10.1002/9781119427339.ch8> (2021).
55. Hoff, P. *A First Course in Bayesian Statistical Methods* (Springer Science & Business Media, 2009).
56. Madadgar, S. & Moradkhani, H. Drought analysis under climate change using copula. *J. Hydrol. Eng.* **18**, 746–759 (2013).
57. Gupta, H. V., Kling, H., Yilmaz, K. K. & Martinez, G. F. Decomposition of the mean squared error and NSE performance criteria: Implications for improving hydrological modelling. *J. Hydrol.* **377**, 80–91 (2009).
58. Xia, Y. et al. Evaluation of multi-model simulated soil moisture in NLDAS-2. *J. Hydrol.* **512**, 107–125 (2014).
59. Gao, X., Avramov, A., Saikawa, E. & Schlosser, C. A. Emulation of Community Land Model Version 5 (CLM5) to quantify sensitivity of soil moisture to uncertain parameters. *J. Hydrometeorol.* **22**, 259–278 (2021).
60. Oloruntoba, B., Kollet, S., Montzka, C., Vereecken, H. & Hendricks Franssen, H.-J. High-resolution land surface modelling over Africa: the role of uncertain soil properties in combination with forcing temporal resolution. *Hydrol. Earth Syst. Sci.* **29**, 1659–1683 (2025).
61. AghaKouchak, A., Cheng, L., Mazdiyasi, O. & Farahmand, A. Global warming and changes in risk of concurrent climate extremes: insights from the 2014 California drought. *Geophys. Res. Lett.* **41**, 8847–8852 (2014).
62. Ahmadalipour, A., Moradkhani, H. & Svoboda, M. Centennial drought outlook over the CONUS using NASA-NEX downscaled climate ensemble. *Int. J. Climatol.* **37**, 2477–2491 (2017).
63. Wells, N., Goddard, S. & Hayes, M. J. A self-calibrating palmer drought severity index. *J. Clim.* **17**, 2335–2351 (2004).
64. Quiring, S. M. Monitoring drought: an evaluation of meteorological drought indices. *Geogr. Compass* **3**, 64–88 (2009).
65. WMO. *Drought Monitoring and Early Warning: Concepts, Progress, and Future Challenges*. WMO-No. 1006 (World Meteorological Organization, 2006).
66. Mankin, J. S. et al. Blue water trade-offs with vegetation in a CO<sub>2</sub>-enriched climate. *Geophys. Res. Lett.* **45**, 3115–3125 (2018).
67. Mankin, J. S., Seager, R., Smerdon, J. E., Cook, B. I. & Williams, A. P. Mid-latitude freshwater availability reduced by projected vegetation responses to climate change. *Nat. Geosci.* **12**, 983–988 (2019).
68. Yu, Z. et al. Global gross primary productivity and water use efficiency changes under drought stress. *Environ. Res. Lett.* **12**, 014016 (2017).
69. Jing, Y., Wang, S., Chan, P. W. & Yang, Z.-L. Gross primary productivity is more sensitive to accelerated flash droughts. *Commun. Earth Environ.* **6**, 34 (2025).
70. Yan, H., DeChant, C. M. & Moradkhani, H. Improving soil moisture profile prediction with the particle filter-Markov chain Monte Carlo method. *IEEE Trans. Geosci. Remote Sens.* **53**, 6134–6147 (2015).
71. Yan, H. & Moradkhani, H. Combined assimilation of streamflow and satellite soil moisture with the particle filter and geostatistical modeling. *Adv. Water Resour.* **94**, 364–378 (2016).
72. Zhang, C. et al. A combined optimization-assimilation framework to enhance the predictive skill of community land model. *Water Resour. Res.* **57**, e2021WR029879 (2021).
73. Abbaszadeh, P., Moradkhani, H. & Yan, H. Enhancing hydrologic data assimilation by evolutionary particle filter and Markov chain Monte Carlo. *Adv. Water Resour.* **111**, 192–204 (2018).
74. Kumar, S. V. et al. Assimilation of remotely sensed soil moisture and snow depth retrievals for drought estimation. *J. Hydrometeorol.* **15**, 2446–2469 (2014).
75. Duan, Q. et al. Model Parameter Estimation Experiment (MOPEX): an overview of science strategy and major results from the second and third workshops. *J. Hydrol.* **320**, 3–17 (2006).
76. Viger, R. J. & Bock, A. *GIS Features of the Geospatial Fabric for National Hydrologic Modeling*. <https://doi.org/10.5066/F7542KMD> (2014).
77. Falcone, J. A. GAGES-II: Geospatial Attributes of Gages for Evaluating Streamflow, Digital Spatial Data Set 2011, available at: [http://water.usgs.gov/GIS/metadata/usgswrd/XML/gagesII\\_Sept2011.xml](http://water.usgs.gov/GIS/metadata/usgswrd/XML/gagesII_Sept2011.xml) (2011).
78. Skamarock, W. C. et al. *A Description of the Advanced Research WRF Version 3* Technical Report NCAR/TN-475+STR (2008).
79. Srivastava, A. K. et al. Assessment of WRF (v 4.2.1) dynamically downscaled precipitation on subdaily and daily timescales over CONUS. *Geosci. Model Dev.* **16**, 3699–3722 (2023).
80. Lawrence, D. et al. *CLM5 Documentation* (2020).
81. Dagon, K., Sanderson, B. M., Fisher, R. A. & Lawrence, D. M. A machine learning approach to emulation and biophysical parameter estimation with the Community Land Model, version 5. *Adv. Stat. Climatol. Meteorol. Oceanogr.* **6**, 223–244 (2020).
82. Elkouk, A. et al. Toward understanding parametric controls on runoff sensitivity to climate in the Community Land Model: a case study

- over the Colorado River Headwaters. *Water Resour. Res.* **60**, e2024WR037718 (2024).
83. Knoben, W. J. M., Freer, J. E. & Woods, R. A. Technical note: inherent benchmark or not? Comparing Nash–Sutcliffe and Kling–Gupta efficiency scores. *Hydrol. Earth Syst. Sci.* **23**, 4323–4331 (2019).
84. Zhang, D. et al. Intensification of hydrological drought due to human activity in the middle reaches of the Yangtze River, China. *Sci. Total Environ.* **637–638**, 1432–1442 (2018).
85. Cai, X. et al. Assessment of simulated water balance from Noah, Noah-MP, CLM, and VIC over CONUS using the NLDAS test bed. *J. Geophys. Res. Atmos.* **119**, 13751–13770 (2014).
86. McKee, T. B., Doeskin, N. J. & Kleist, J. The relationship of drought frequency and duration to time scales. In: *Proc. 8th Conference on Applied Climatology* 179–184 (Colorado State University, 1993).
87. Hulley, G. C., Dousset, B. & Kahn, B. H. Rising Trends in Heatwave Metrics Across Southern California. *Earth's Futur.* **8**, e2020EF001480 (2020).
88. Fullerton, A. H., Sun, N., Baerwalde, M. J., Hawkins, B. L. & Yan, H. Mechanistic simulations suggest riparian restoration can partly counteract climate impacts to juvenile salmon. *J. Am. Water Resour. Assoc.* **58**, 525–546 (2022).
89. Böhnisch, A., Felsche, E., Mittermeier, M., Poschlod, B. & Ludwig, R. Future patterns of compound dry and hot summers and their link to soil moisture droughts in Europe. *Earth's Futur.* **13**, e2024EF004916 (2025).
90. Allen, R. G., Pereira, L. S., Raes, D., Smith, M. Crop Evapotranspiration—Guidelines for Computing Crop Water Requirements—FAO Irrigation and Drainage Paper. FAO1998). D05109.
91. Naresh Kumar, M., Murthy, C. S., Sessa Sai, M. V. R. & Roy, P. S. On the use of Standardized Precipitation Index (SPI) for drought intensity assessment. *Meteorol. Appl.* **16**, 381–389 (2009).
92. Hosking, J. R. M. & Wallis, J. R. *Regional Frequency Analysis: An Approach Based on L-Moments* (Cambridge University Press, 1997).
93. Yan, H. & Moradkhani, H. A regional Bayesian hierarchical model for flood frequency analysis. *Stoch. Environ. Res. Risk Assess.* **29**, 1019–1036 (2015).
94. Dai, M. et al. Propagation characteristics and mechanism from meteorological to agricultural drought in various seasons. *J. Hydrol.* **610**, 127897 (2022).
95. Liu, X., Peng, J., Liu, Y., Yu, S. & Wang, Y. The Three Gorges Dam has weakened the drought propagation process in the Yangtze River Basin. *J. Hydrol.* **632**, 130875 (2024).
96. Hoerling, M. et al. Causes and predictability of the 2012 Great Plains drought. *Bull. Am. Meteorol. Soc.* **95**, 269–282 (2014).
97. Christian, J. I. et al. Global projections of flash drought show increased risk in a warming climate. *Commun. Earth Environ.* **4**, 165 (2023).
98. Yevjevich, V. *An Objective Approach to Definitions and Investigations of Continental Hydrologic Drought* (Colorado State University, 1967).
99. Tu, X. et al. Bivariate design of hydrological droughts and their alterations under a changing environment. *J. Hydrol. Eng.* **24**, (2019).
100. Huang, S. et al. Drought propagation modification after the construction of the Three Gorges Dam in the Yangtze River Basin. *J. Hydrol.* **603**, 127138 (2021).
101. Joe, H. *Multivariate Models and Dependence Concepts* (Routledge, 1997).
102. Nelsen, R. B. *An Introduction to Copulas* (Springer, 1999).
103. Madadgar, S. & Moradkhani, H. A Bayesian framework for probabilistic seasonal drought forecasting. *J. Hydrometeorol.* **14**, 1685–1705 (2013).
104. Salvadori, G., De Michele, C., Kottegoda, N. T. & Rosso, R. *Extremes in Nature: An Approach Using Copulas* (2007).
105. Sklar, A. Fonctions de répartition à n dimensions et leurs marges. *Publ. l'Institut Stat. l'Université Paris* **8**, 229–231 (1959).
106. Madadgar, S. & Moradkhani, H. Copula function and drought. in *Handbook of Drought and Water Scarcity, Vol. 1: Principles of Drought and Water Scarcity* (Francis and Taylor, 2016).
107. Genest, C. & Rémillard, B. Validity of the parametric bootstrap for goodness-of-fit testing in semiparametric models. *Ann. l'IHP Probab. Stat.* **44**, 1096–1127 (2008).
108. Sadegh, M., Ragno, E. & AghaKouchak, A. Multivariate Copula Analysis Toolbox (MvCAT): Describing dependence and underlying uncertainty using a Bayesian framework. *Water Resour. Res.* **53**, 5166–5183 (2017).
109. Casella, G. & Berger, R. L. *Statistical Inference*. vol. 2 (Duxbury Thompson Learning, 2002).
110. Peng, Y., Shi, Y., Yan, H. & Zhang, J. Multivariate frequency analysis of annual maxima suspended sediment concentrations and floods in the Jinsha River, China. *J. Hydrol. Eng.* **25**, (2020).
111. Yan, H. & Moradkhani, H. Toward more robust extreme flood prediction by Bayesian hierarchical and multimodeling. *Nat. Hazards* **81**, 203–225 (2016).

## Acknowledgements

This research was supported by the U.S. Department of Energy (DOE), Office of Science, as part of research in MultiSector Dynamics, Earth, and Environmental System Modeling Program. This research used resources of the National Energy Research Scientific Computing Center (NERSC), a DOE Office of Science User Facility located at Lawrence Berkeley National Laboratory, operated under Contract No. DE-AC02-05CH11231 using NERSC award BER-ERCAP0027385. We thank the three anonymous reviewers whose constructive comments and suggestions helped improve the quality and clarity of the manuscript.

## Author contributions

H.Y. conceived the study, conducted the formal analysis, and led the writing of the manuscript. N.S. and L.Y. contributed to the investigation and provided critical review and editing of the manuscript. T.T. developed and maintained the software used in the analysis. J.R. secured funding and provided overall project administration. All authors have read and approved the final version of the manuscript.

## Competing interests

The authors declare no competing interests.

## Additional information

**Supplementary information** The online version contains supplementary material available at <https://doi.org/10.1038/s44304-025-00134-y>.

**Correspondence** and requests for materials should be addressed to Hongxiang Yan.

**Reprints and permissions information** is available at <http://www.nature.com/reprints>

**Publisher's note** Springer Nature remains neutral with regard to jurisdictional claims in published maps and institutional affiliations.

**Open Access** This article is licensed under a Creative Commons Attribution 4.0 International License, which permits use, sharing, adaptation, distribution and reproduction in any medium or format, as long as you give appropriate credit to the original author(s) and the source, provide a link to the Creative Commons licence, and indicate if changes were made. The images or other third party material in this article are included in the article's Creative Commons licence, unless indicated otherwise in a credit line to the material. If material is not included in the article's Creative Commons licence and your intended use is not permitted by statutory regulation or exceeds the permitted use, you will need to obtain permission directly from the copyright holder. To view a copy of this licence, visit <http://creativecommons.org/licenses/by/4.0/>.

© Battelle Memorial Institute 2025